Article

A membrane-based seawater electrolyser for hydrogen generation

https://doi.org/10.1038/s41586-022-05379-5

Received: 6 January 2022

Accepted: 21 September 2022

Published online: 30 November 2022

Check for updates

Heping Xie[1,2]✉, Zhiyu Zhao[2], Tao Liu[2], Yifan Wu[2], Cheng Lan[2], Wenchuan Jiang[2], Liangyu Zhu[3], Yunpeng Wang[4], Dongsheng Yang[5] & Zongping Shao[6,7]✉

Electrochemical saline water electrolysis using renewable energy as input is a highly desirable and sustainable method for the mass production of green hydrogen[1–7]; however, its practical viability is seriously challenged by insufficient durability because of the electrode side reactions and corrosion issues arising from the complex components of seawater. Although catalyst engineering using polyanion coatings to suppress corrosion by chloride ions or creating highly selective electrocatalysts has been extensively exploited with modest success, it is still far from satisfactory for practical applications[8–14]. Indirect seawater splitting by using a pre-desalination process can avoid side-reaction and corrosion problems[15–21], but it requires additional energy input, making it economically less attractive. In addition, the independent bulky desalination system makes seawater electrolysis systems less flexible in terms of size. Here we propose a direct seawater electrolysis method for hydrogen production that radically addresses the side-reaction and corrosion problems. A demonstration system was stably operated at a current density of 250 milliamperes per square centimetre for over 3,200 hours under practical application conditions without failure. This strategy realizes efficient, size-flexible and scalable direct seawater electrolysis in a way similar to freshwater splitting without a notable increase in operation cost, and has high potential for practical application. Importantly, this configuration and mechanism promises further applications in simultaneous water-based effluent treatment and resource recovery and hydrogen generation in one step.

The key point of our strategy is the integration of an in situ water purification process based on a self-driven phase transition mechanism into seawater electrolysis, which is realized by applying a hydrophobic porous polytetrafluoroethylene (PTFE)-based waterproof breathable membrane as a gas-path interface and adopting concentrated potassium hydroxide (KOH) solution as a self-dampening electrolyte (SDE) (Fig. 1a). Such a design allows the biased diffusion of water vapour but fully prevents the penetration of liquid seawater and impurity ions. During operation, the difference in water vapour pressure between the seawater and the SDE across the membrane provides a driving force for spontaneous seawater gasification (evaporation) at the seawater side and the diffusion of water vapour through the short gas path inside the membrane to the SDE side, where it is re-liquified by absorption by the SDE. This phase transition migration process allows the in situ generation of pure water for electrolysis from a seawater source with 100% ion-blocking efficiency, while the water consumed by simultaneous electrolysis in the SDE successfully maintains the interface pressure difference. Therefore, when the water migration rate equals the electrolysis rate, a new thermodynamic equilibrium is established between the seawater and the SDE, and continuous and stable water migration through a 'liquid–gas–liquid' mechanism is realized to provide fresh water for electrolysis (Fig. 1b).

To confirm the feasibility of our seawater electrolysis concept, we first established a lab-scale seawater electrolysis system (SES) with a symmetrical structure for investigating the electrochemical performance (Extended Data Fig. 1a). The electrocatalyst layers were fixed to the electrode plates, and a hydrophilic diaphragm was used to separate the two electrodes and prevent the mixing of hydrogen (H_2) and oxygen (O_2). The SDE storage frame has the function of providing an SDE environment and fixing the porous PTFE membrane, in which water migration happens at the bottom and generated gas is released at the top to avoid the potential loss of H_2. Moreover, the PTFE membrane completely separates the SDE and seawater. The SES steadily operated to produce H_2 from seawater (Shenzhen Bay, China; Supplementary Table 1) for over 72 h with average voltages of approximately 1.95 V and 2.3 V at current densities of 250 mA cm^{-2} and 400 mA cm^{-2}, respectively (Fig. 1c). With long-term continuous seawater consumption during the electrolysis process, there was a

[1]Guangdong Provincial Key Laboratory of Deep Earth Sciences and Geothermal Energy Exploitation and Utilization, Institute of Deep Earth Sciences and Green Energy, College of Civil and Transportation Engineering, Shenzhen University, Shenzhen, China. [2]Institute of New Energy and Low-Carbon Technology, Sichuan University, Chengdu, China. [3]Petroleum Engineering School, Southwest Petroleum University, Chengdu, China. [4]School of Chemical Engineering, Sichuan University, Chengdu, China. [5]College of Polymer Science and Engineering, Sichuan University, Chengdu, China. [6]State Key Laboratory of Materials-Oriented Chemical Engineering, College of Chemical Engineering, Nanjing Tech University, Nanjing, China. [7]WA School of Mines: Minerals, Energy and Chemical Engineering, Curtin University, Perth, Western Australia, Australia. ✉e-mail: xiehp@scu.edu.cn; shaozp@njtech.edu.cn

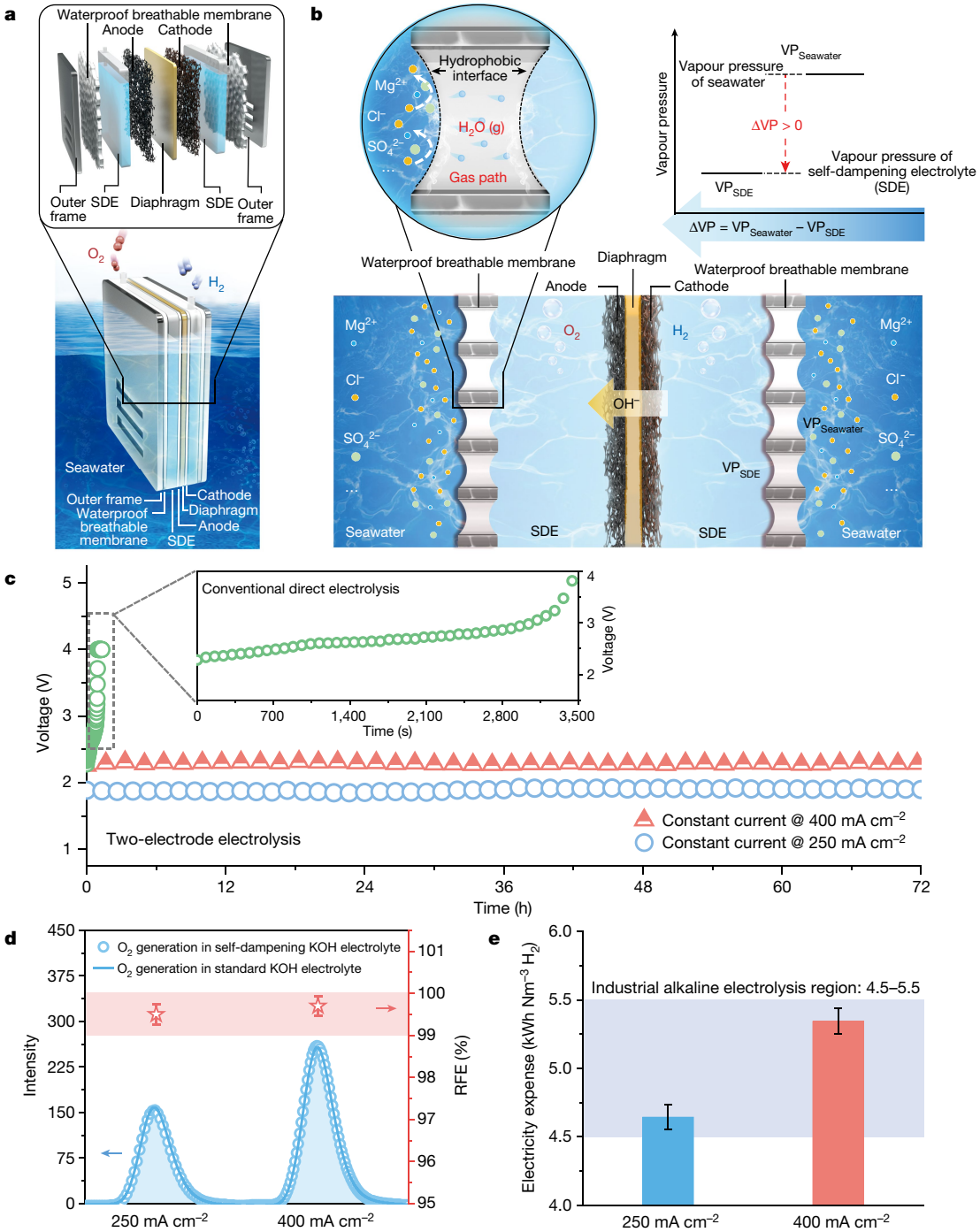

Fig. 1 | Design of the SES. a, Schematic diagram of a typical SES. **b**, The liquid–gas–liquid phase transition-based migration mechanism of the water purification and migration process and the driving force. **c**, Electrolysis durability test at constant current densities of 250 mA cm^{-2} and 400 mA cm^{-2} in Shenzhen Bay seawater for a total period of 72 h. The inset shows the electrolysis durability test of conventional direct seawater splitting in seawater with commercial electrocatalysts. **d**, The RFEs of O_2 generation at 250 mA cm^{-2} and 400 mA cm^{-2} in the SDE, obtained based on gas chromatography measurements of the O_2 formation rate; three measurements were conducted for each data point with the error bars corresponding to the standard deviation. **e**, A comparison of the current SES with industrial alkaline electrolysis in terms of electricity expense; three measurements were conducted for each data point with the error bars corresponding to the standard deviation.

gradual drop in the seawater level in the container (Extended Data Fig. 1b), indicating that the water molecules in the seawater migrated to the SDE side. Gas chromatography analysis shows that the relative Faradaic efficiency (RFE) at both 250 mA cm^{-2} and 400 mA cm^{-2} was nearly 100% for O_2 generation without chlorine (Cl_2) evolution (Fig. 1d). In addition, as expected, very low concentrations of impurity ions, that is, 0.074 mg l^{-1} ClO^-, 0.082 mg l^{-1} SO_4^{2-} and 0.062 mg l^{-1} Mg^{2+}, were detected in the SDE after 72 h of continuous water electrolysis at 400 mA cm^{-2}, which were only 0.008‰, 0.052‰ and 0.089‰ the concentrations of the corresponding ions in seawater (Extended Data Fig. 1c). These results strongly support sustainable H_2 generation based on a liquid–gas–liquid phase transition-based water migration mechanism for in situ water purification in seawater electrolysis. Calculations show that the electricity expense of H_2 production is

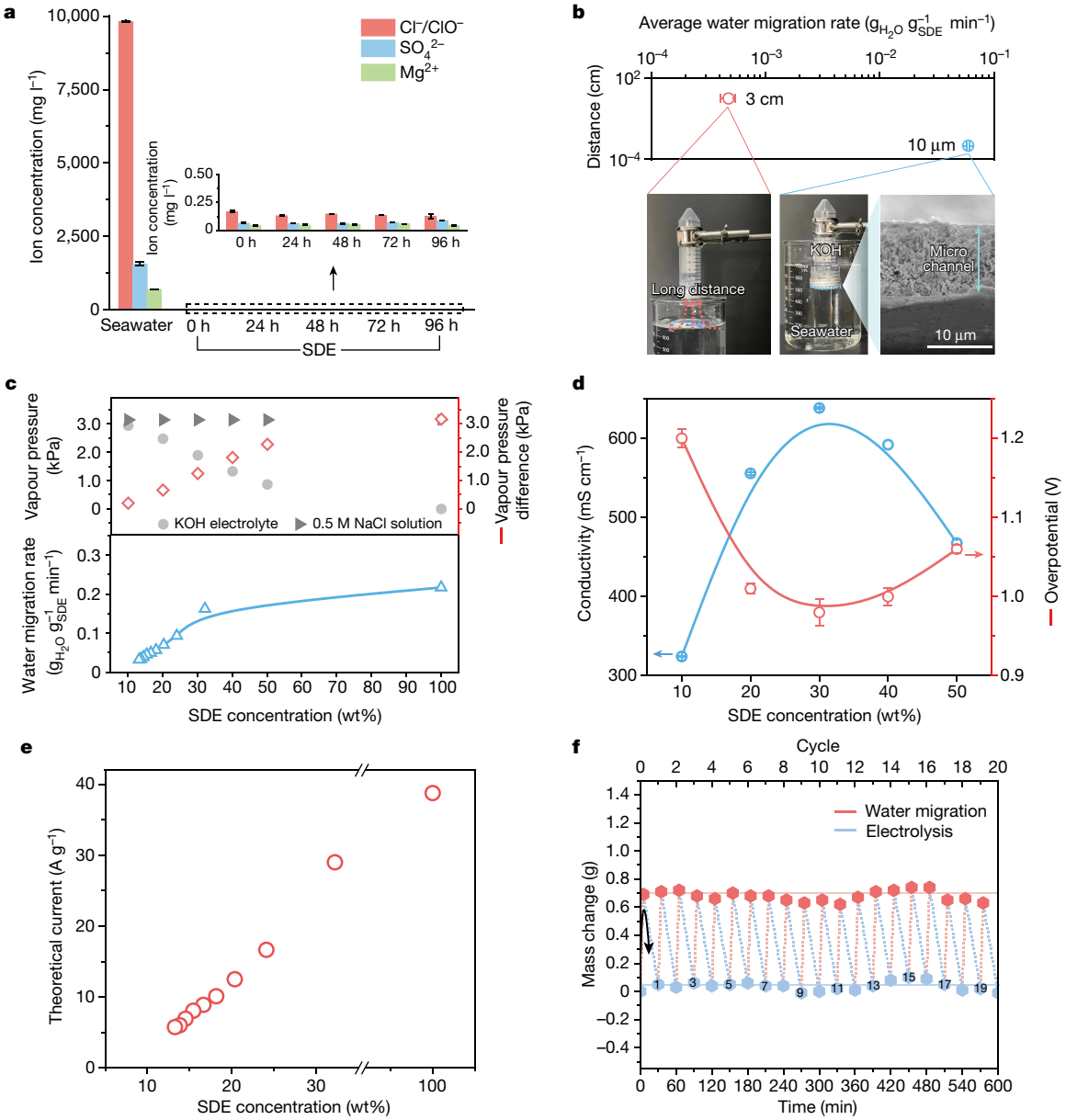

Fig. 2 | Origin of continuous and highly efficient electrolysis. a, Ion concentration in the SDE over time. Each mean value was calculated from three measurements with the error bars corresponding to the standard deviation. **b**, Average water migration rate under different molecular diffusion distances, showing that the micrometre-scale directional gas path enhances the water migration rate by approximately two orders of magnitude. In addition, mass transfer in seawater can avoid carbon dioxide absorption. Each mean value was calculated from four measurements with the error bars corresponding to the standard deviation. **c**, Relationship between the water migration rate and water vapour pressure difference between the seawater and the SDE. **d**, Relationship between overpotential (current density of 250 mA cm^{-2}, in a typical electrolytic cell) and SDE conductivity (KOH solution) at different concentrations. Each mean value was calculated from three measurements with the error bars corresponding to the standard deviation. **e**, Variation in the maximum electrolytic theoretical current provided by a certain water migration rate under different KOH electrolyte concentrations. The theoretical values of current (I) corresponding to the instantaneous water migration rate under various SDE concentrations can be defined as $I = nZF/t$. **f**, Static equilibrium test of SDE over multiple cycles.

approximately 4.6 kWh Nm^{-3} H_2 and 5.3 kWh Nm^{-3} H_2 at current densities of 250 mA cm^{-2} and 400 mA cm^{-2}, respectively, which is comparable to that of industrial alkaline electrolysis with pure water[22], owing to the elimination of a separate desalination process (Fig. 1e, Extended Data Fig. 1d and Supplementary Table 2). In contrast, direct electrolysis of seawater by the conventional method caused serious electrocatalyst corrosion, and electrolysis failed within 1 h of operation, accompanied by the formation of milky-white flocculent precipitates (Fig. 1c and Extended Data Fig. 1e). Very recently, the incorporation of a forward osmosis membrane into a seawater electrolyser to extract water from seawater and into the electrolyte was reported[6,7]. In that study, an ion-selective hydrophilic semipermeable membrane was used to block the diffusion of impurity ions from seawater to the electrolyte, while the concentration gradient on both sides of the membrane acted as the driving force for water migration in a liquid state from seawater with lower concentration to the electrolyte with a higher concentration. However, noticeable mutual ion diffusion between the seawater and the electrolyte was still observed within 24–120 h of operation, suggesting a non-ideal ion-sieving effect of the membrane. The leaking of ions from the electrolyte into seawater may cause an additional

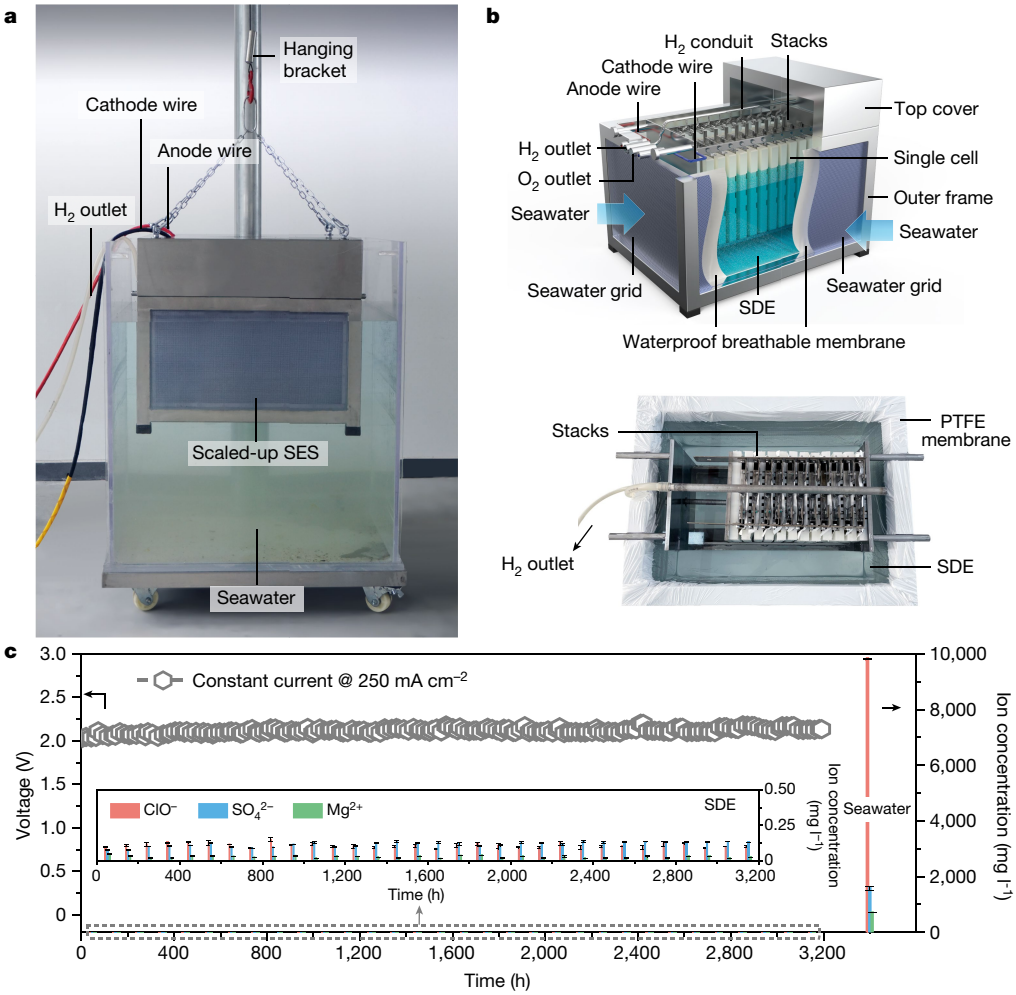

Fig. 3 | Scale-up and generality. a, Optical image of a scaled-up SES for direct seawater electrolysis. **b**, Schematic of the scaled-up SES. **c**, Electrolysis durability test for the scaled-up SES at a constant current density of 250 mA cm^{-2}. Each mean value of ion concentration was calculated from three measurements with the error bars corresponding to the standard deviation.

problem of seawater pollution. In addition, relatively poor electrolysis performance was observed owing to a neutral electrolyte being required to ensure the stability of the membrane.

Here the hydrophobic porous PTFE membrane introduces a tightly connected micrometre-scale gas diffusion path between the seawater and the SDE to directionally transport water vapour and fully prevent liquid penetration. Mass transfer across this gas path occurs through a liquid–gas–liquid phase transition; that is, liquid water evaporates to form a gas phase on the seawater side and migrates across the membrane in the state of gaseous water; it liquefies again by absorption by the SDE. The multiple fluorine structure of PTFE has a low surface energy, forming superhydrophobic isolation domains to inhibit the permeation of seawater and ions over time (Extended Data Fig. 2a,b and Supplementary Fig. 1). As expected, the concentrations of the various ions (ClO^-, SO_4^{2-} and Mg^{2+}) in the SDE remained stable within 96 h and were all at least four orders of magnitude lower than those in seawater (Fig. 2a). The micrometre-scale gas path immersed in water accelerated the generation of water vapour and increased its migration rate by at least two orders of magnitude compared with those obtained with longer water diffusion paths, such as absorbing water vapour above the sea surface (Fig. 2b). Favourably, this microporous structure can withstand a maximum pressure of approximately 0.74 MPa at 0.1-μm pore size, which is equivalent to the pressure at approximately 75-m seawater depth (Extended Data Fig. 2c and Supplementary Table 3). The water migration rate was found to be significantly dependent on the membrane properties. A larger gas-path area facilitated more water vapour migration to the SDE during a certain period (Extended Data Fig. 2d and Supplementary Fig. 2a). In addition, intermolecular collisions and collisions between molecules and membrane pores took place simultaneously, in which a larger pore size and shorter gas-path length both accelerated the water migration rate (Extended Data Fig. 2e,f and Supplementary Fig. 2b,c). The scanning electron microscopy (SEM) images show that the PTFE membrane pores were negligibly blocked after 15 d of electrolysis in Shenzhen Bay seawater (Extended Data Fig. 6a,b), suggesting the outstanding antifouling capability of the PTFE membrane. Regardless, for much longer operation periods, the risk of membrane wetting and fouling still needs to be taken into serious consideration[17,23,24].

An SDE with a low saturated water vapour pressure, high ionic conductivity and high electrochemical stability within the water-splitting window plays an important role in the consecutive liquid–gas–liquid phase transition-based water migration process, providing a successive driving force to enhance water migration from seawater to the SDE without extra energy consumption (Extended Data Fig. 3a). In addition, when the water vapour reaches the SDE, it is re-liquified by hydration and absorption processes by the SDE[25] (Extended Data Fig. 3b). Interestingly, numerous electrolytes possess SDE-like functions, such as KOH, potassium carbonate (K_2CO_3) and tripotassium phosphate (K_3PO_4) (Supplementary Fig. 3). In general, an SDE undergoes four stages in the self-dampening process: dry crystals, a mixture

of crystals and saturated solution, a saturated solution, and a dilute solution[26]. The SDE concentration will gradually decrease with water capture, accompanied by variations in conductivity. For example, without electrolysis, the KOH (SDE) concentration decreased from 100 wt% to 13.3 wt% after the SES was immersed in simulated seawater (0.5 M sodium chloride (NaCl)) for 90 min (Extended Data Fig. 3c). The water migration rate decreased with a reduction in SDE concentration in the absence of electrolysis, owing to the gradually decreased interfacial water vapour pressure difference (Fig. 2c). During this process, the ion conductivity of the KOH solution increased dramatically to a peak of 638 mS cm^{-1} at approximately 30 wt% SDE and then declined with the migration of more water into the SDE (Fig. 2d). In addition, the electrolysis performance was closely related to the KOH concentration (Fig. 2d and Extended Data Fig. 3d). Here, 30 wt% KOH can be considered the optimal SDE as it has the highest conductivity, providing attractive electrochemical performance, and creates a reasonable difference in water vapour pressure from that of seawater to realize a favourable water migration rate.

To further understand the process of continuous seawater electrolysis for sustainable H_2 generation in an SES based on a liquid–gas–liquid phase transition-based water migration mechanism, we built a model balancing water migration and water consumption by electrolysis according to Darcy's and Faraday's laws (as shown in Methods). When external condition parameters (membrane parameters, temperature and so on) are defined, the model can be described as a function of the water vapour pressure difference, which is directly related to the solution concentration. The SES can realize operational balance when the rates of water migration and electrolysis reach equilibrium, which further confirms that continuous and stable H_2 production can be achieved by adjusting the SDE concentration and current value if the seawater concentration is constant. We then calculated the maximum theoretical current value of the SES under different SDE concentrations (Fig. 2e). The results showed that the theoretical current reaches approximately 5.8 A g^{-1} to 38.8 A g^{-1} when the KOH concentration ranges from 13.3 wt% to 100 wt%. This result suggests that the amount of water migration per unit time induced by 1 g KOH is enough for water electrolysis at a high current. An SES can be considered a dynamic balance system. If the initial electrolysis rate is higher than the water migration rate $\left(\left(\frac{dM}{dt}\right)_{\text{electrolysis}} > \left(\frac{dM}{dt}\right)_{\text{migration}}\right)$ (where t and M are time and water mass, respectively), the SDE concentration increases, leading to an increase in the water vapour pressure difference (ΔP); consequently, the water migration rate increases to match the electrolysis rate to reach a dynamic balance. If $\left(\frac{dM}{dt}\right)_{\text{electrolysis}} < \left(\frac{dM}{dt}\right)_{\text{migration}}$, the SDE concentration decreases, causing a reduction in ΔP; consequently, the water migration rate decreases to match the electrolysis rate until a new balance is reached. In actual operation, equilibrium between the water migration rate and consumption rate, that is, $\left(\frac{dM}{dt}\right)_{\text{electrolysis}} = \left(\frac{dM}{dt}\right)_{\text{migration}}$, can be reached at the initial stage of operation if the membrane parameters and SDE concentration are properly set.

The static equilibrium performance of the SES was further evaluated by a multiple-cycle experiment. Each cycle consisted of water migration for 5 min, followed by 25 min of electrolysis under a 4-A current. The SES exhibited good stability for at least 20 cycles without an obvious degradation in performance (Fig. 2f), showing sustainable cyclability and the potential for stable electrolysis. Thus, when the water migration amount induced by the interface pressure difference and the water consumption amount of electrolysis reach a dynamic balance per unit time, the system is able to provide a stable 'in situ water purification–electrolysis' process, enabling continuous and efficient H_2 production from seawater.

A COMSOL simulation using an ideal porous gas-path system with simulated seawater (0.5 M NaCl) and an SDE (30 wt% KOH) on the two sides further revealed spatiotemporal insights into the water migration process. We began by modelling the water migration process from seawater to the SDE through a gas path using previously established models (Methods). The simulations predicted the water migration potential at different depths (0–2,000 m) and temperatures (0 °C, 10 °C, 20 °C and 30 °C) to broaden the adaptability of our strategy to various ocean depths and seasonal climates. Temperature greatly affects the water vapour pressure, and the initial migration rate at 30 °C is approximately 6 times that at 0 °C. Water migration still appears at 0 °C, suggesting the feasibility of our system for operating at low temperature (as shown in Extended Data Fig. 4a–d). At different seawater depths, the vapour pressure of seawater needs to be considered as a function of both temperature and pressure (Extended Data Fig. 4e). The water vapour pressure difference varies significantly with depth in the thermocline layer owing to the notable temperature changes in this area. In addition, in principle, even at a 2,000-m depth, there is still a driving force between the SDE and seawater, indicating the feasibility of H_2 generation in the deep ocean based on this water phase transition migration strategy. However, the mechanical strength and breakthrough pressure of the membrane would be a new concern owing to the need to withstand the high pressure in the deep ocean.

To demonstrate the practical applicability of our approach, we further fabricated a demo-type SES at a 386 l h^{-1} H_2 generation scale (Fig. 3a). As shown in Fig. 3b and Extended Data Fig. 5a, the system is compact with dimensions of only 82 cm × 62 cm × 70.5 cm and consists of 11 cells with a total effective geometric surface area of 3,696 cm^2 for each electrode (H_2 evolution electrode and O_2 evolution electrode). We compared the voltages at different current densities between the scaled-up SES and lab-scale SES. As shown in Extended Data Fig. 5b and Supplementary Fig. 4, the voltage of the scaled-up SES increased by a certain degree compared with that of the lab-scale SES at the corresponding current density, which may be caused by increasing contact resistance during system amplification. At a constant current density of 250 mA cm^{-2} for electrolysis with Shenzhen Bay seawater, the scaled-up SES still exhibited outstanding stable performance for over 3,200 h with an energy consumption of approximately 5.0 kWh Nm^{-3} H_2 (Fig. 3c and Supplementary Figs. 5 and 6). In addition, no obvious increase in impurity ions (ClO^-, SO_4^{2-} and Mg^{2+}) was detected in the SDE after long-term operation, and the concentrations of all three ions were still at least four orders of magnitude lower than those in seawater (suggesting 100% ion-blocking efficiency), indicating that there was almost no membrane wetting or liquid penetration even in the large-scale electrolyser during the long operation period. Indeed, SEM revealed that the catalyst layer maintained its original morphology after long-term electrolysis and was not obviously corroded in the pure electrolytic environment (Extended Data Fig. 6c,d). Thus, our scalable system has a great potential for use in the energy construction of ecological floating islands owing to its compact design, limited system engineering and excellent performances.

To demonstrate the versatility of our strategy, we also performed a 24-h stability test of our system with different solid hygroscopic SDEs, including poly(2-acrylamide-2-methylpropanesulfonic acid (PAMPS) and polyvinyl alcohol/KOH (PVA/KOH) hydrogels, with the results shown in Extended Data Fig. 7. With the PVA/KOH hydrogel, the system exhibited a superior electrolysis performance of 1.85 V and 250 mA cm^{-2} owing to its hydrophilicity and high ionic conductivity. We further studied the electrolysis performance by using various electrocatalysts. A current density of 250 mA cm^{-2} was achieved at an overpotential of 410 mV for a synthesized molybdenum-doped nickel sulfide/nickle foam (Mo-Ni_3S_2/NF) electrocatalyst, and the SES constructed with the above electrocatalyst operated stably for at least 100 h with 30 wt% KOH (SDE) (Extended Data Fig. 8). Moreover, a conductive hydrophobic breathable membrane with superior antifouling performance is highly desirable for our strategy, as it may be directly integrated into the electrode to perform an additional function as a current collector.

These improvements may further optimize the structure and reduce energy consumption to make this approach more suitable for energy-intensive industrial systems in the future. In addition to seawater, the strategy is applicable to other non-volatile liquids, such as highly concentrated acid, alkali and salt solutions (Extended Data Fig. 9), to realize industrial wastewater treatment. Moreover, it may be used for simultaneous H_2 production and the recovery of useful resources in water, such as for lithium enrichment. As a proof of concept, 0.07 M lithium chloride (LiCl) solution was selected as the water source; the concentration of the Li^+ solution increased from 0.07 M to 2.92 M after water migration and electrolysis for more than 204 h, and lithium carbonate (Li_2CO_3) crystals precipitated after adding K_2CO_3 (Extended Data Fig. 10).

In conclusion, we have demonstrated a scalable, side-reaction-free and corrosion-free direct seawater splitting strategy that realizes in situ self-driven water purification and water electrolysis in a single system. The key technology is the incorporation of a self-breathable waterproof membrane and an SDE into the electrolyser. Owing to the difference in water vapour pressure between seawater and the SDE, water migration from the seawater across the membrane to the SDE is self-driven through a liquid–gas–liquid phase transition mechanism. This unique water purification mechanism ensures 100% ion-blocking efficiency, the hydrophobic nature of the membrane results in anti-fouling capability and the micrometre-scale gas diffusion path enables a high water migration rate. As a practical demonstration of this approach, a lab-scale SES was operated stably over 72 h with near 100% RFE. The scaled-up SES with a H_2 generation capability of 386 l h^{-1} was stably operated at 250 mA cm^{-2} for over 3,200 h with an attractively low energy consumption of 5.0 kWh Nm^{-3} H_2, and no obvious electrocatalyst corrosion or membrane wetting was observed. By applying a solid hygroscopic SDE and a lower-overpotential catalyst, this strategy may be adaptable to energy-intensive industrial production in the future and could be used for effluent treatment and resource recovery coupled with one-step H_2 generation. We foresee that further broadening of this phase-transition-based water migration strategy will lead to the development of advanced H_2 production from seawater or impure water for practical applications.

Online content

Any methods, additional references, Nature Portfolio reporting summaries, source data, extended data, supplementary information, acknowledgements, peer review information; details of author contributions and competing interests; and statements of data and code availability are available at https://doi.org/10.1038/s41586-022-05379-5.

1. Nishiyama, H. et al. Photocatalytic solar hydrogen production from water on a 100-m^2 scale. *Nature* **598**, 304–307 (2021).
2. Dresp, S., Dionigi, F., Klingenhof, M. & Strasser, P. Direct electrolytic splitting of seawater-opportunities and challenges. *ACS Energy Lett.* **4**, 933–942 (2019).
3. Jin, H., Wang, X., Tang, C., Vasileff, A. & Qiao, S. Stable and highly efficient hydrogen evolution from seawater enabled by an unsaturated nickel surface nitride. *Adv. Mater.* **33**, 2007508 (2021).
4. Karunadasa, H. I. et al. A molecular MoS_2 edge site mimic for catalytic hydrogen generation. *Science* **335**, 698–702 (2012).
5. Shi, L. et al. Using reverse osmosis membranes to control ion transport during water electrolysis. *Energy Environ. Sci.* **13**, 3138–3148 (2020).
6. Veroneau, S. S. & Nocera, D. G. Continuous electrochemical water splitting from natural water sources via forward osmosis. *Proc. Natl Acad. Sci. USA* **118**, e2024855118 (2021).
7. Veroneau, S. S., Hartnett, A. C., Thorarinsdottir, A. E. & Nocera, D. G. Direct seawater splitting by forward osmosis coupled to water electrolysis. *ACS Appl. Energy Mater.* **5**, 1403–1408 (2022).
8. Kuang, Y. et al. Solar-driven, highly sustained splitting of seawater into hydrogen and oxygen fuels. *Proc. Natl Acad. Sci. USA* **116**, 201900556 (2019).
9. Sun, F., Qin, J. & Wang, Z. Energy-saving hydrogen production by chlorine-free hybrid seawater splitting coupling hydrazine degradation. *Nat. Commun.* **12**, 4182 (2021).
10. Dresp, S., Thanh, T. N., Klingenhof, M., Brueckner, S. & Strasser, P. Efficient direct seawater electrolysers using selective alkaline NiFe-LDH as OER catalyst in asymmetric electrolyte feeds. *Energy Environ. Sci.* **13**, 1725–1729 (2020).
11. Yu, L., Zhu, Q., Song, S., Mcelhenny, B. & Ren, Z. Non-noble metal-nitride based electrocatalysts for high-performance alkaline seawater electrolysis. *Nat. Commun.* **10**, 5106 (2019).
12. Miao, J., Xiao, F. X., Yang, H. B., Khoo, S. Y. & Liu, B. Hierarchical Ni–Mo–S nanosheets on carbon fiber cloth: a flexible electrode for efficient hydrogen generation in neutral electrolyte. *Sci. Adv.* **1**, 1500259 (2015).
13. Dinh, C. T. et al. Multi-site electrocatalysts for hydrogen evolution in neutral media by destabilization of water molecules. *Nat. Energy* **4**, 107–114 (2019).
14. Tong, W. et al. Electrolysis of low-grade and saline surface water. *Nat. Energy* **5**, 367–377 (2020).
15. Loutatidou, et al. Capital cost estimation of RO plants: GCC countries versus southern Europe. *Desalination* **347**, 103–111 (2014).
16. Caldera, U. & Breyer, C. Learning curve for seawater reverse osmosis desalination plants: capital cost trend of the past, present and future. *Water Resour. Res.* **53**, 10523–10538 (2017).
17. Choudhury, M. R., Anwar, N., Jassby, D. & Rahaman, M. S. Fouling and wetting in the membrane distillation driven wastewater reclamation process—a review. *Adv. Colloid Interface Sci.* **269**, 370–399 (2019).
18. Ahmad, N. A., Goh, P. S., Yogarathinam, L. T., Zulhairun, A. K. & Ismail, A. F. Current advances in membrane technologies for produced water desalination. *Desalination* **493**, 114643 (2020).
19. Generous, M. M., Qasem, N., Akbar, U. A. & Zubair, S. M. Techno-economic assessment of electrodialysis and reverse osmosis desalination plants. *Sep. Purif. Technol.* **272**, 118875 (2021).
20. Wang, M. et al. Ultrafast seawater desalination with covalent organic framework membranes. *Nat. Sustain.* **5**, 518–526 (2022).
21. Jones, E., Qadir, M., van Vliet, M. T., Smakhtin, V. & Kang, S.-M. The state of desalination and brine production: a global outlook. *Sci. Total. Environ.* **657**, 1343–1356 (2019).
22. Ursua, A., Gandia, L. M. & Sanchis, P. Hydrogen production from water electrolysis: current status and future trends. *Proc. IEEE* **100**, 410–426 (2012).
23. Yin, Y., Jeong, N. & Tong, T. The effects of membrane surface wettability on pore wetting and scaling reversibility associated with mineral scaling in membrane distillation. *J. Membr. Sci.* **614**, 118503 (2020).
24. Qiu, H. et al. Functional polymer materials for modern marine biofouling control. *Prog. Polym. Sci.* **127**, 101516 (2022).
25. Yang, K. et al. A roadmap to sorption-based atmospheric water harvesting: from molecular sorption mechanism to sorbent design and system optimization. *Environ. Sci. Technol.* **55**, 6542–6560 (2021).
26. Tereshchenko, & Anatoly, G. Deliquescence: hygroscopicity of water-soluble crystalline solids. *J. Pharm. Sci.* **104**, 3639–3652 (2015).

Methods

Materials

The materials used in this study included KOH (Adamas, >90%), sulfuric acid (Adamas, 96%), NaCl (Greagent, 99.5%), *N,N'*-methylenebisacrylamide (Sigma Aldrich, 99%), 2-acrylamide-2-methylpropanesulfonic acid (Adamas, 98%), ammonium persulfate (Adamas, 98%), polyvinyl alcohol 1799 (Kelong), $Na_2MoO_4{\cdot}2H_2O$ (Aladdin, 99%), CH_4N_2S (Aladdin, 99%), $Ni(CH_3COO)_2{\cdot}4H_2O$ (Aladdin), several porous PTFE membranes with different pore sizes (0.1 μm, 0.45 μm, 1 μm, 3 μm and 5 μm pore sizes according to commercial specifications; JCMSC, Hunan Lujing Environmental Technology), commercial porous MoNi/NF catalyst (aperture 85 ppi, area density 450 g m^{-2}; Kunshan Guangjiayuan Electronic Materials), commercial PtNi mesh catalyst (the substrate mesh was woven with nickel wire with a diameter of 0.15 mm, Luzhou Hongjiang Electrolytic Equipment).

Synthesis of PAMPS and PVA/KOH hygroscopic SDEs

The PAMPS hygroscopic SDE was synthesized by free radical polymerization. Stoichiometric amounts of 2-acrylamide-2-methylpropanesulfonic acid (AMPS), *N,N'*-methylenebisacrylamide (MBA) and ammonium persulfate (APS) were dissolved in deionized water to form a precursor solution, which was bubbled with nitrogen gas for at least 10 min. The precursor solution was then injected into a PTFE reaction container, which was kept at ambient temperature for 24 h to ensure completion of the reaction. The resulting PAMPS hygroscopic SDE was immersed into pure water to remove the residuals and subsequently immersed into polyethylene glycol to remove water. Then the SDE was used for H_2 production and played a key role in inducing water vapour liquefaction and proton and water migration.

For PVA/KOH, a 10 wt% PVA solution was prepared by dissolving PVA 1799 particles in deionized water under vigorous stirring and heating (70 °C). A 10-wt% PVA aqueous precursor was poured into a PTFE container. The container was cooled at −20 °C. The frozen PVA solution was then immersed into 40-wt% KOH solution for up to 24 h. Then the PVA/KOH hygroscopic SDE was obtained. In the H_2 production process, the PVA/KOH was used to induce water vapour liquefaction and OH^- ion migration.

Synthesis of the Mo-Ni_3S_2/NF anode electrocatalyst

The Mo-Ni_3S_2/NF anode electrocatalyst was reported in our previous work[27], and was synthesized in the laboratory. In a typical synthesis, $Ni(CH_3COO)_2{\cdot}4H_2O$ (1 mmol), $Na_2MoO_4{\cdot}2H_2O$ (1 mmol), CH_4N_2S (3 mmol) and 15 ml deionized water were continuously stirred until dissolution. After that, the mixed solution and treated nickel foams were transferred into a Teflon-lined stainless autoclave and maintained at 160 °C for 6 h. After cooling to room temperature, the electrocatalyst samples were obtained, repeatedly washed with deionized water and ethanol, and then vacuum dried at 60 °C for several hours.

Material characterization

The micromorphology of the gas path in the PTFE membrane was observed with an SEM (Thermo Scientific Apreo 2C). Fourier transform infrared spectroscopy was performed with a Nicolet 6700 spectrophotometer over the wavenumber range 4,000–400 cm^{-1} to characterize the structure of the PTFE membrane. The water contact angle of the PTFE membrane was measured using a contact angle goniometer (DSA 25, Krüss) with deionized water and seawater drops at room temperature. The breakthrough pressure of the PTFE membrane was measured with a high-pressure flat membrane tester (FlowMem0021-HP). The morphology of the commercial catalyst was observed with an SEM (JEOL JSM-7500F). Surface elemental mapping was performed using a focused ion beam SEM instrument (FEI Helios G4 UC).

Water migration behaviour and vapour pressure simulation

Water migration behaviour was observed by determining weight variations of the SDE at 25 °C. Here KOH and 0.5 M NaCl were considered the SDE and simulated seawater, respectively. A certain amount of KOH solid (or solution) and 0.5 M NaCl were placed on both sides of the PTFE membrane. The KOH weight change was recorded at intervals to prepare a plot of water migration mass with time. Here we measured the water migration behaviour with different areas, path lengths and membrane pore sizes, and different simulated solution (seawater, acid, alkali and salt) concentrations. In addition, the water vapour pressure of KOH with different concentrations and simulated seawater (0.5 M NaCl) were calculated with Aspen Plus.

Ion concentration characterization

The concentrations of Cl^-, SO_4^{2-} and Mg^{2+} in seawater and the SDE were measured by ion chromatography (Thermo Scientific ICS100) and inductively coupled plasma-optical emission spectrometry (PE Avio 200). The hypochlorite (ClO^-) concentration in the SDE was measured by the *o*-tolidine method via a redox reaction between hypochlorite and *o*-tolidine[9]. The test solution was 0.5 mmol *o*-tolidine in deionized water. To obtain a calibration curve, different amounts of ClO^- (0 μM, 6 μM, 12 μM, 24 μM, 36 μM and 60 μM) were added to KOH solutions (0.1 ml) and injected into the testing solution. The ultraviolet–visible spectra were measured to obtain a plot of absorbance at a wavelength of 436 nm versus ClO^- concentration. After long-term electrolysis, SDE (0.1 ml) was added to the testing solution, and the ClO^- concentration was determined by comparing the spectrum with the calibration curve.

Electrolysis performance testing

KOH SDE solutions with different concentrations (10 wt%, 20 wt%, 30 wt%, 40 wt% and 50 wt%) were first prepared. The conductivity of the SDE was then measured with a conductivity metre (INESA, DDBJ-351L) with platinum plate electrodes at room temperature. The electrocatalytic properties of the electrocatalysts were measured with an electrochemical workstation (CHI660, CH Instruments). Linear sweep voltammetry or cyclic voltammetry was conducted between 0 V and 2.7 V with a constant flow of nitrogen gas in the electrolyte during the experiment to eliminate dissolved O_2. The linear sweep voltammograms of the lab-scale SES and scaled-up SES were measured with a multimetre. The corresponding voltages between the anode and cathode plates were obtained at various current densities of 0 mA cm^{-2}, 10 mA cm^{-2}, 50 mA cm^{-2}, 100 mA cm^{-2}, 150 mA cm^{-2}, 200 mA cm^{-2} and 250 mA cm^{-2}.

Electrolysis durability test

Durability tests were performed for the seawater electrolysis process with a power supply (ITECH, IT6900A) operating at a constant current density of 250 mA cm^{-2} or 400 mA cm^{-2}. The actual electrolyser voltage was recorded as the final result. The RFE was determined by the actual amount of O_2 formation as measured by gas chromatography. During a test, an electrochemical workstation was used to maintain stable O_2 generation with different current densities. Nitrogen was purged into the anodic chamber at a fixed flow rate, and the chamber was connected to the gas-sampling loop of a gas chromatograph (Shimadzu, GC-2014C). A thermal conductivity detector was used to detect and quantify the amount of O_2 generated. The RFE was defined as the ratio of O_2 produced in the KOH self-dampening electrolyte to the amount of O_2 produced in a standard alkaline water electrolyser with KOH electrolyte[8].

For SES cycle stability testing, we measured the water migration behaviour of the SDE over 5 min with a 9.6-cm^2 membrane area and subsequent electrolysis desorption for 25 min under a 4-A constant current. All procedures were the same as above, and the measurement was repeated 20 times.

Comparison with conventional direct seawater splitting

For comparison, conventional seawater splitting using commercial catalysts (MoNi/NF for the anode and PtNi mesh for the cathode) was also carried out with Shenzhen Bay seawater. As shown in Extended Data Fig. 1, the anode rapidly shed and dissolved, leading to rapid failure of the electrolysis within 1 h. In addition, milky-white flocculent precipitates appeared in the seawater shortly after the start of electrolysis, indicating localized formation of a higher pH[28]. These results suggested that seawater splitting requires an engineered system and that the membrane modules, electrolytes and catalysts of the electrolysers must operate in a clear and pure electrolyte environment. Our strategy based on the liquid–gas–liquid phase transition migration mechanism thus provides many unique and advanced advantages. (1) The isolated interface of the micrometre-scale gas-phase path in seawater for liquid–gas–liquid continuous mass transfer avoids impurity penetration over time, provides a pure environment for electrolysis, eliminates various potential side reactions and protects the electrolyser system. It is essentially different from using reverse osmosis or forward osmosis to obtain pure water. (2) The micrometre-scale gas-path shortens the migration length of water vapour and supplies sufficient water in situ for H_2 generation, which permits effective electrolysis and uninterrupted H_2 production. (3) Water migration in SES is a spontaneous process, which requires less energy consumption than energy-intensive desalination processes such as reverse osmosis or membrane distillation. (4) The compact design of the SES might facilitate reductions in system engineering, maintenance, required land space and capital costs.

Energy consumption associated with H_2 production

To compare the electricity expenses for H_2 production, we calculated the average energy consumption per Nm^3 of H_2. The total energy consumption of the actual electrolysis process, W, was calculated as follows:

$$W = I \times \int U \mathrm{d}t$$

where I is the current and U is the voltage. Next, the volume of H_2 produced, V, was calculated as follows:

$$V = 22.4 \times I \times t/(Z \times F)$$

where the number of electrons transferred for the hydrogen evolution reaction, Z, is 2 and the Faraday constant, F, is 96,485 C mol^{-1}. Thus, the energy consumption is $Q = W/V$ (kWh Nm^{-3}).

H_2 production coupled with lithium enrichment

A LiCl (0.07 M) feed solution was prepared. Before concentrating the Li^+, a K_2CO_3 solution (0.8 M) was mixed with the feed solution, and there was no precipitation. Water migrated from the LiCl solution for H_2 generation at a constant current of 400 mA cm^{-2}. After electrolysis, the 0.8 M K_2CO_3 solution was used to precipitate Li^+, and the sample was further centrifuged, filtered, dried and pulverized to obtain the Li_2CO_3 product.

Assembly of the lab-scale SES

The lab-scale SES has a symmetrical structure in which both sides contain a catalyst layer, electrode plate, SDE storage frame and outer frame, and the two sides are separated by a diaphragm to separate H_2 and O_2. Commercial porous MoNi/NF and PtNi mesh catalysts (about 1 mm thickness) were utilized for the anode and cathode catalyst layers, respectively (Supplementary Fig. 7). The electrode plates were made of stainless steel, and a groove (3.5 × 3.5 cm^2) was carved under them to place the catalyst layer. The catalyst area can be adjusted from 1 × 1 cm^2 to 3.5 × 3.5 cm^2 according to the actual situation. Three 0.5 × 3.5 cm^2 through-holes were evenly distributed in the groove for SDE diffusion and gas release. The SDE storage frames were made of transparent polymethyl methacrylate. Grooves of 5.3 × 6.8 cm^2 and 6 × 8 cm^2 area were provided at the centres of the front and back sides to insert electrode plates and PTFE membranes. The PTFE membrane was located adjacent to both electrodes, and each side the effective water migration area was 3 × 2 cm^2. There were chambers inside the frames for SDE storage, which were also connected with the groovesmentioned above. The upper part of the chamber was used for transferring the SDE to the electrocatalyst surface, and the bottom of the chamber had an effective area of 3 × 2 cm^2 to allow the SDE to closely contact the PTFE membrane and obtain pure water.

Assembly of the scaled-up SES

The scaled-up SES consisted of an outer frame (70.5 cm × 82 cm × 62 cm) and inner-core electrolysis stacks. The lower part of the outer frame was provided with porous grids to pass seawater. The PTFE membrane was lined on the five inner walls of the electrolyser box (except for the top) to create a gas path in the seawater and hold the KOH solution (SDE) at the same time. This assembly method was slightly different from that of a lab-scale SES, which facilitates quick and efficient assembly and integration in the scaled-up device. In addition, we set a relatively large gas path interface area to provide more water migration mass and solve the problems such as water evaporation caused by heat generated after enlarging the system. The core electrolysis stacks were composed of 11 independent cells in parallel, and each cell included a positioning frame, anode electrode plate, anode catalyst layer, diaphragm and cathode. The positioning frame (33 cm × 26 cm × 2.5 cm) was made of PTFE, and the through-hole was used for mass transfer of the SDE and diffusion of O_2. The anode electrode plate was made of stainless steel, and a 1-mm-deep groove was carved under the plate to insert the porous anode catalyst layer (24 cm × 14 cm). The diaphragm (30 cm × 20 cm) was utilized for separating H_2 and O_2. There was a PtNi mesh (24 cm × 14 cm) on the surface of the cathode, and the generated H_2 was discharged through the gas conduit above the cathode.

Model construction for phase transition migration and continuous H_2 production

The theoretical model was based on the following assumptions. (1) In the instantaneous process, temperature changes, thermal convection and concentration polarization on both sides of the membrane are not considered. (2) The amount of water migration per unit time is equal to that absorbed by the KOH solution (SDE) for the same area and time.

According to Darcy's law, the water migration mass flux is assumed to be proportional to the vapour pressure difference across the PTFE membrane and is given by:

$$J(x) = B_\mathrm{m}\Delta P = B_\mathrm{m}[P_\mathrm{s} - P(x)] \quad (1)$$

where x is the molar fraction of substance, $J(x)$ is the mass flux (g m^{-2} s^{-1}), B_m is the membrane permeability (g m^{-2} s^{-1} Pa^{-1}) and P_s and $P(x)$ are the water vapour pressures at the seawater and the SDE side surfaces (Pa), respectively.

The governing quantity that indicates which mechanism is operative under a given experimental condition is the Knudsen number, K_n, which is defined as the ratio of the mean free path (λ) of the transported molecules to the pore size (diameter, $2r$) of the membrane, that is, $K_\mathrm{n} = \lambda/2r$ (ref. [29]).

For $K_\mathrm{n} > 1$ or $r < 0.5\lambda$, the membrane pore size is smaller than the mean free path of the vapour molecules, and thus molecule–pore wall collisions are dominant. Under this condition, B_m can be calculated by[29,30]:

$$B_\mathrm{m} = B_\mathrm{m}^K = \frac{2r}{3}\frac{\varepsilon}{\tau\delta}\frac{M_\mathrm{w}}{RT}\left(\frac{8RT}{\pi M_\mathrm{w}}\right)^{1/2} \quad (2)$$

For $K_\mathrm{n} < 0.01$ or $r > 50\lambda$, the membrane pores are much larger than the free path of water vapour, which means that molecule–pore wall

collisions are negligible, and ordinary molecular diffusion is utilized to demonstrate this mass transport in the continuum region. In light of this, B_m can be calculated with[9,30]:

$$B_m = B_m^D = \frac{\varepsilon}{\tau\delta}\frac{M_w}{RT}\left(\frac{P_{pore}D}{P_{air}}\right) \tag{3}$$

For $0.01 < K_n < 1$ or $0.5\lambda < r < 50\lambda$, intermolecular collisions and collisions between molecules and membrane pores take place simultaneously, and B_m can be calculated with[29,30]:

$$B_m = B_m^C = \left(\frac{1}{B_m^K} + \frac{1}{B_m^D}\right)^{-1} = \frac{\varepsilon}{\tau\delta}\frac{M_w}{RT}\frac{1}{\frac{3}{2r}\left(\frac{\pi M_w}{8RT}\right)^{1/2} + \left(\frac{P_{air}}{P_{pore}D}\right)} \tag{4}$$

In the above equations, ε is the porosity of the membrane, τ is the membrane tortuosity, δ is the thickness of the membrane (m), r is the pore radius of the membrane (m), M_w is the molecular weight of the water vapour (g mol^{-1}), R is the ideal gas constant (8.314 J mol^{-1} K^{-1}), T is the temperature (K), P_{air} is the air pressure within the membrane pores (Pa), P_{pore} is the total pressure inside the pores (Pa) and D is the diffusion coefficient (m^2 s^{-1}).

The membrane tortuosity can be calculated with[31]:

$$\tau = \frac{(2-\varepsilon)^2}{\varepsilon} \tag{5}$$

Certain variables in the permeability equation are calculated as follows[32]:

$$P_{avg} = [P_s + P(x)]/2 \tag{6}$$

$$P_{air} = P_{pore} - P_{avg} \tag{7}$$

where P_{avg} is the average pressure in the membrane pores (Pa).

The diffusivity of water vapour through the stagnant air inside the pores is given by[33,34]:

$$P_{pore}D = 1.895 \times 10^{-5} T^{2.072} \tag{8}$$

Seawater can be considered a NaCl solution. The water vapour pressure on the seawater side can be calculated with[35]:

$$P_s = (1 - x_s) \times (1 - 0.5x_s - 10x_s^2) \times \exp\left[23.1964 - \frac{3816.44}{T - 46.13}\right] \tag{9}$$

where x_s is the molar fraction of NaCl.

The water vapour pressure on the SDE side can be calculated with[36]:

$$\begin{aligned}\log\left(\frac{P(x)}{10^5}\right) = &\left[-0.01508 \times \left(\frac{55.56x}{1-x}\right) - 0.0016788 \times \left(\frac{55.56x}{1-x}\right)^2 \right.\\ &\left. + 2.25887 \times 10^{-5} \times \left(\frac{55.56x}{1-x}\right)^3\right]\\ &+ \left[1 - 0.0012062 \times \left(\frac{55.56x}{1-x}\right)\right.\\ &+ 5.6024 \times 10^{-4} \times \left(\frac{55.56x}{1-x}\right)^2\\ &\left. - 7.8228 \times 10^{-6}\left(\frac{55.56x}{1-x}\right)^3\right]\\ &\times \left(35.4462 - \frac{3343.93}{T} - 10.9\log T + 0.0041645T\right)\end{aligned} \tag{10}$$

where, x is the molar fraction of KOH.

The water migration rate can be calculated with:

$$\left(\frac{dM}{dt}\right)_{migration} = J(x)S = B_m[P_s - P(x)]S \tag{11}$$

where S is the water migration area (m^2). The water electrolysis rate can be calculated with equations (12) and (13):

$$It = nZF \tag{12}$$

$$\left(\frac{dM}{dt}\right)_{electrolysis} = \frac{18I}{ZF} \tag{13}$$

where n is the amount of substance (mol). I is the current (A), Z is the number of electrons transferred for the hydrogen evolution reaction and F is the Faraday constant (96,485 C mol^{-1}).

When the rates of water migration and electrolysis are equal, the SES becomes balanced.

$$\frac{dM}{dt} = \left(\frac{dM}{dt}\right)_{migration} - \left(\frac{dM}{dt}\right)_{electrolysis} = B_m[P_s - P(x)]S - \frac{18I}{ZF} \tag{14}$$

COMSOL simulations

To demonstrate our strategy in various spatiotemporal environments, we carried out COMSOL simulations to investigate water migration behaviour at seasonal temperatures (0 °C, 10 °C, 20 °C and 30 °C) and the potential of interface driving force at various seawater depths. The modelling and governing equations are based on the previous section. To mimic water migration originating from seawater, seawater is modelled with 0.5 M NaCl solution, and the amount and concentration of seawater are assumed to be always constant during the process of migration. The parameters for the submerged gas path are set as follows: the thickness is 60 μm, the area is 1×1 m^2, the porosity is 90% and the pore size is 1 μm. The SDE is considered to be a 30-wt% KOH solution, and its temperature vary with the seasons. At different depths, the influences of temperature and hydraulic pressure on water vapour pressure need to be considered. The temperature (T) at various depths can be calculated with[37,38]:

$$T = \begin{cases} 298.15 & (-20 \le h \le 0) \\ 298.15 + 0.04(h+20) & (-345 \le h \le -20) \\ 274.45 + 10.7\exp\left[\dfrac{0.335 - (-h - 344.888)^{0.5}}{20}\right] & (-2,000 \le h \le -345) \end{cases} \tag{15}$$

where h is the seawater depth (m).

The effect of hydraulic pressure on vapour pressure (P_w) is expressed by the following formula[39]:

$$P_w = P_{w_0} \times \exp\left(\frac{M_w g|h|}{RT}\right) \tag{16}$$

where P_{w_0} is the water vapour pressure at ambient pressure and temperature (Pa), M_w is the molecular weight (kg mol^{-1}), R is the ideal gas constant (8.314 J mol^{-1} K^{-1}), T is the temperature (K), g is gravitational acceleration (m s^{-2}) and h is the seawater depth (m).

Data availability

The data that support the findings of this study are available from the corresponding authors upon reasonable request.

27. Lan, C., Xie, H., Wu, Y., Chen, B. & Liu, T. Nanoengineered, Mo-doped, Ni_3S_2 electrocatalyst with increased Ni–S coordination for oxygen evolution in alkaline seawater. *Energy Fuels* **36**, 2910–2917 (2022).
28. Hausmann, J. N., Schlögl, R., Menezes, P. & Driess, M. Is direct seawater splitting economically meaningful? *Energy Environ. Sci.* **14**, 3679–3685 (2021).
29. Qtaishat, M., Matsuura, T., Kruczek, B. & Khayet, M. Heat and mass transfer analysis in direct contact membrane distillation. *Desalination* **219**, 272–292 (2008).
30. Matsuura, T. *Synthetic Membranes and Membrane Separation Processes* (CRC, 2020).
31. Iversen, S. B., Bhatia, V. K., Dam-Johansen, K. & Jonsson, G. Characterization of microporous membranes for use in membrane contactors. *J. Membr. Sci.* **130**, 205–217 (1997).
32. Khalifa, A., Ahmad, H., Antar, M., Laoui, T. & Khayet, M. Experimental and theoretical investigations on water desalination using direct contact membrane distillation. *Desalination* **404**, 22–34 (2017).
33. Phattaranawik, J., Jiraratananon, R. & Fane, A. G. Effect of pore size distribution and air flux on mass transport in direct contact membrane distillation. *J. Membr. Sci.* **215**, 75–85 (2003).
34. Khayet, M., Velázquez, A. & Mengual, J. I. Modelling mass transport through a porous partition: effect of pore size distribution. *J. Non Equilibrium Thermodyn.* **29**, 279–299 (2004).
35. Lawson, K. W. & Lloyd, D. R. Membrane distillation. *J. Membr. Sci.* **124**, 1–25 (1997).
36. Balej, J. Water vapour partial pressures and water activities in potassium and sodium hydroxide solutions over wide concentration and temperature ranges. *Int. J. Hydrogen Energy* **10**, 233–243 (1985).
37. Chu, P. C., Fan, C. & Liu, W. T. Determination of vertical thermal structure from sea surface temperature. *J. Atmos. Ocean. Technol.* **17**, 971–979 (2000).
38. Levitus, S. & Boyer, T. P. *World Ocean Atlas 1994. Volume 4. Temperature* (National Environmental Satellite, Data, and Information Service, 1994).
39. Straub, A. P., Yip, N. Y., Lin, S., Lee, J. & Elimelech, M. Harvesting low-grade heat energy using thermo-osmotic vapour transport through nanoporous membranes. *Nat. Energy* **1**, 16090 (2016).

Acknowledgements This work is supported by the National Natural Science Foundation of China (grant numbers 52004166, 52104400 and 51827901) and the Science and Technology Department of Sichuan Province (grant number 2020YFH0012). We thank the Program for Guangdong Introducing Innovative and Entrepreneurial Teams (grant number 2019ZT08G315), and we thank the Institute of New Energy and Low-Carbon Technology, Sichuan University for support.

Author contributions H.X., T.L. and Z.S. conceived and designed the project. Z.Z., Y.W. and C.L. performed the characterizations and experiments. Z.Z., T.L., W.J. and Y.W. analysed the data. L.Z. and D.Y. designed the devices. H.X., Z.Z., T.L., Y.W. and Z.S. drafted the article and revised it critically. All authors reviewed the manuscript.

Competing interests The authors declare no competing interests.

Additional information

Supplementary information The online version contains supplementary material available at https://doi.org/10.1038/s41586-022-05379-5.

Correspondence and requests for materials should be addressed to Heping Xie or Zongping Shao.

Peer review information *Nature* thanks Marcel Risch and the other, anonymous, reviewer(s) for their contribution to the peer review of this work.

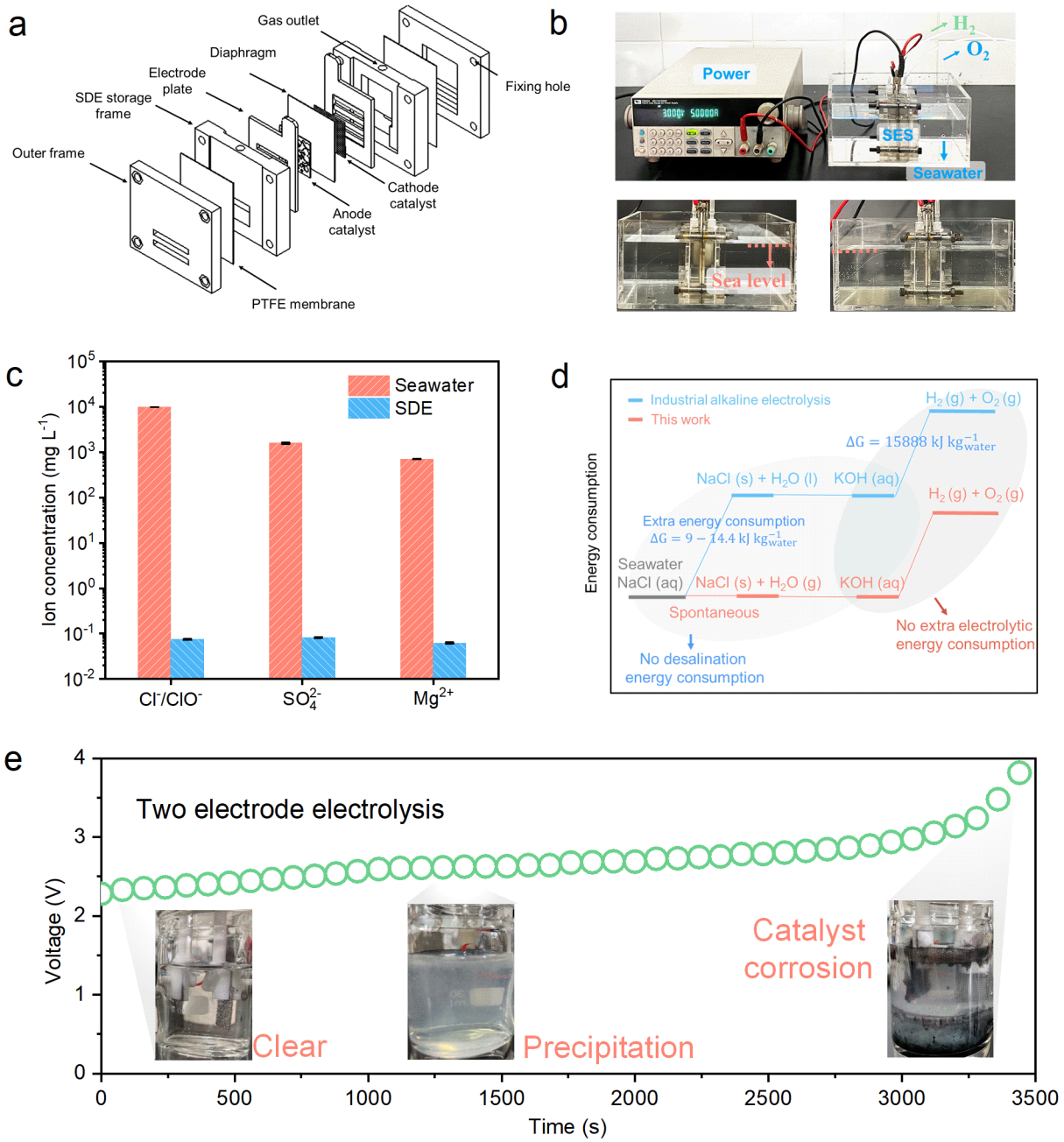

Extended Data Fig. 1 | In situ seawater splitting of SES and conventional seawater direct splitting. a, A schematic diagram of the lab-scale SES. **b**, Photos of the lab-scale SES and operation process. **c**, Ion chromatography tests show that the gas path can prevent seawater penetration, so the ion content in SDE is still nearly four orders of magnitude lower than that in seawater after long-term electrolysis. **d**, The energy consumption analysis. From the whole period, assuming that the water source is seawater, it is necessary to desalination before use in industrial alkaline electrolysis, which needs to consume at least 9–14.4 kJ kg^{-1}_{water}, while the phase transition of SES is a spontaneous process, which saves the energy of desalination. During electrolysis, the energy input of our strategy is equivalent to industrial alkaline water electrolysis when the system conditions are the same, which has been confirmed above. **e**, Electrolysis durability test of conventional direct seawater (Shenzhen Bay seawater) splitting with commercial electrocatalysts. The inset shows photos of clear seawater before electrolysis, precipitation in seawater during electrolysis, and catalyst electrode dissolving and shedding in seawater after electrolysis.

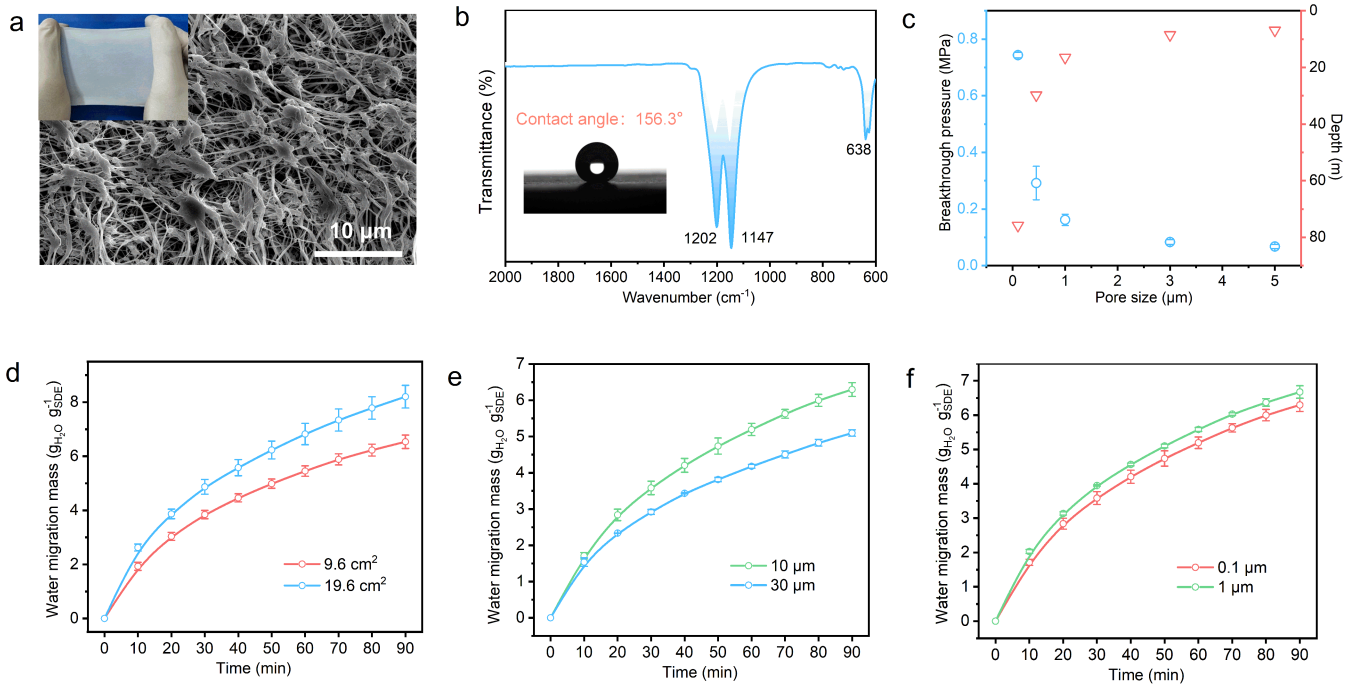

Extended Data Fig. 2 | Characteristics of the PTFE membrane and directional gas path. a, Photograph and SEM images of the PTFE membrane. **b**, Fourier transform infrared spectroscopy (FTIR) result shows different chemical vibration bonds of PTFE. The two bands located at 1147 and 1202 cm^{-1} are assigned to the -CF_2 stretching vibrations of PTFE, and the 638 cm^{-1} peak is the -CF_2 wagging vibrations of PTFE. Due to the large electronegativity and small radius of F atoms, the PTFE membrane has a lower surface energy, thus resulting in an excellent hydrophobic characteristic. The inset demonstrates the superhydrophobic property of the PTFE membrane, and the average droplet contact angle in air was measured as 156.3°. Each mean value was calculated from five measurements. **c**, The breakthrough pressure and corresponding theoretical hydrostatic depth of the PTFE membrane with different pore sizes. The curve of water migration mass over time at different membrane areas (**d**), gas path lengths (**e**) and pore sizes (**f**). In this process, the electrolysis reaction was not involved. Each mean value was calculated from three measurements.

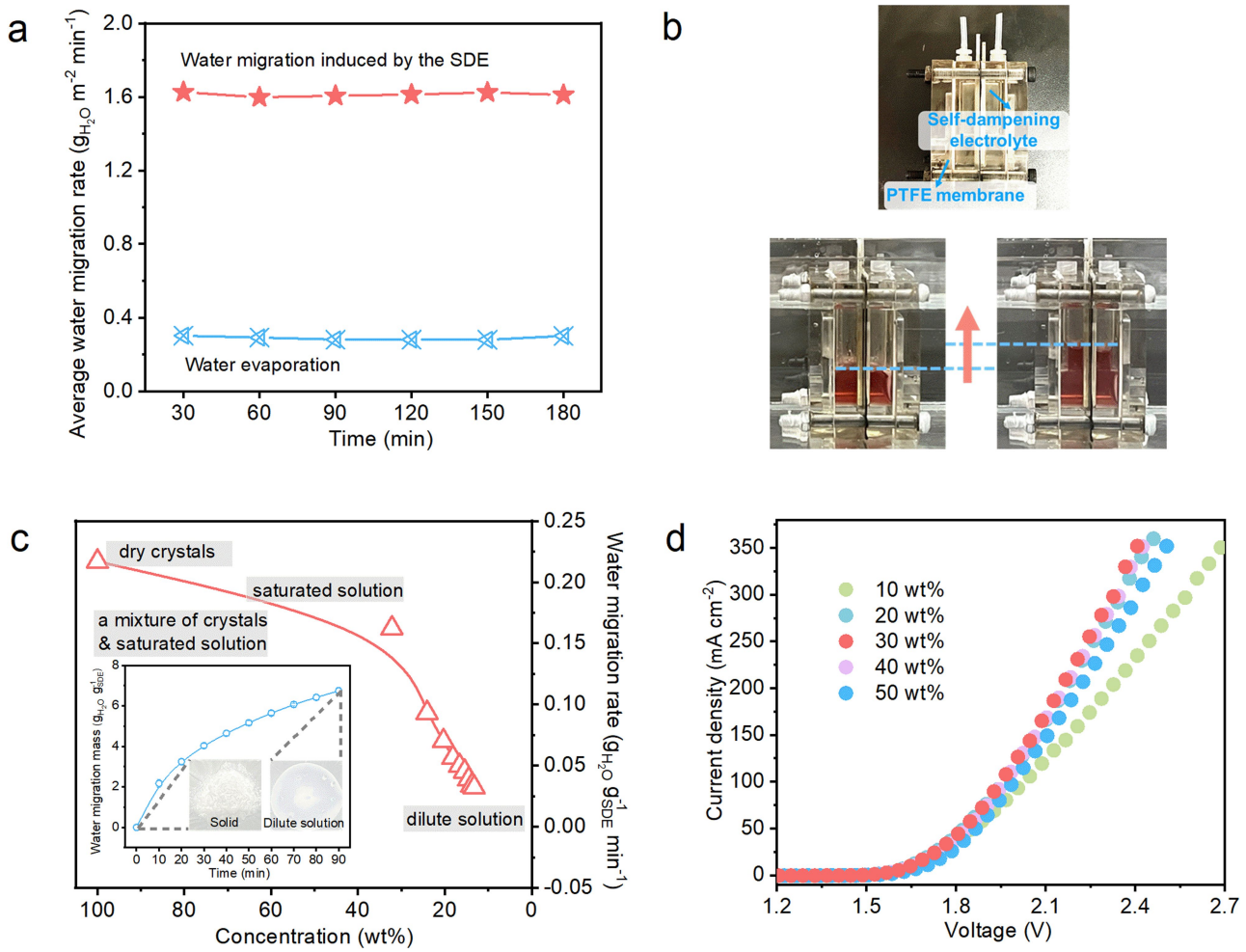

Extended Data Fig. 3 | Water phase transition migration from seawater to the SDE. a, The average migration rate curve of water showing a fast migration rate induced by KOH electrolyte (SDE) under a vapour pressure difference. **b**, Photograms of the phase transition migration of seawater. **c**, The relationship curve of the water migration rate and SDE concentration. The inset shows the amount of water migration in simulated seawater (under conditions of 1 μm pore size and 9.6 cm^2 gas path area, KOH solid as initial SDE). **d**, LSV scans of commercial catalysts (MoNi/NF anode paired with a PtNi mesh cathode) taken in various concentrations of KOH solution (SDE) at room temperature.

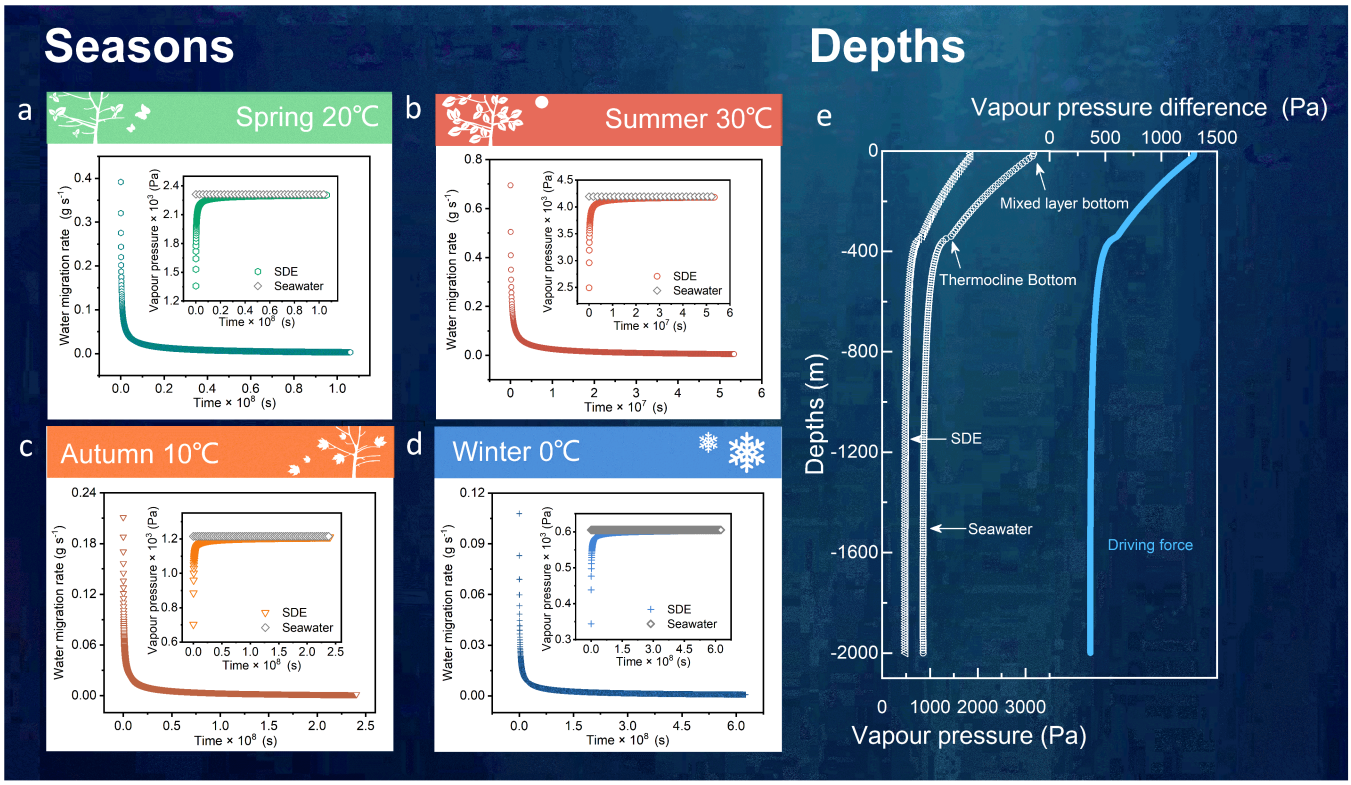

Extended Data Fig. 4 | Spatiotemporal adaptivity. a–**d**, Water migration rate from seawater to 30-wt% KOH electrolyte (SDE) in various seasons (the average temperature is considered to be 20 °C-spring, 30 °C-summer, 10 °C-autumn and 0 °C-winter). The inset demonstrates that at different seasonal temperatures the water vapour pressure of the SDE generally increases with water migration until it is equal to that of the seawater side. **e**, The curve shows the variation in water vapour pressure and water vapour pressure difference with depths.

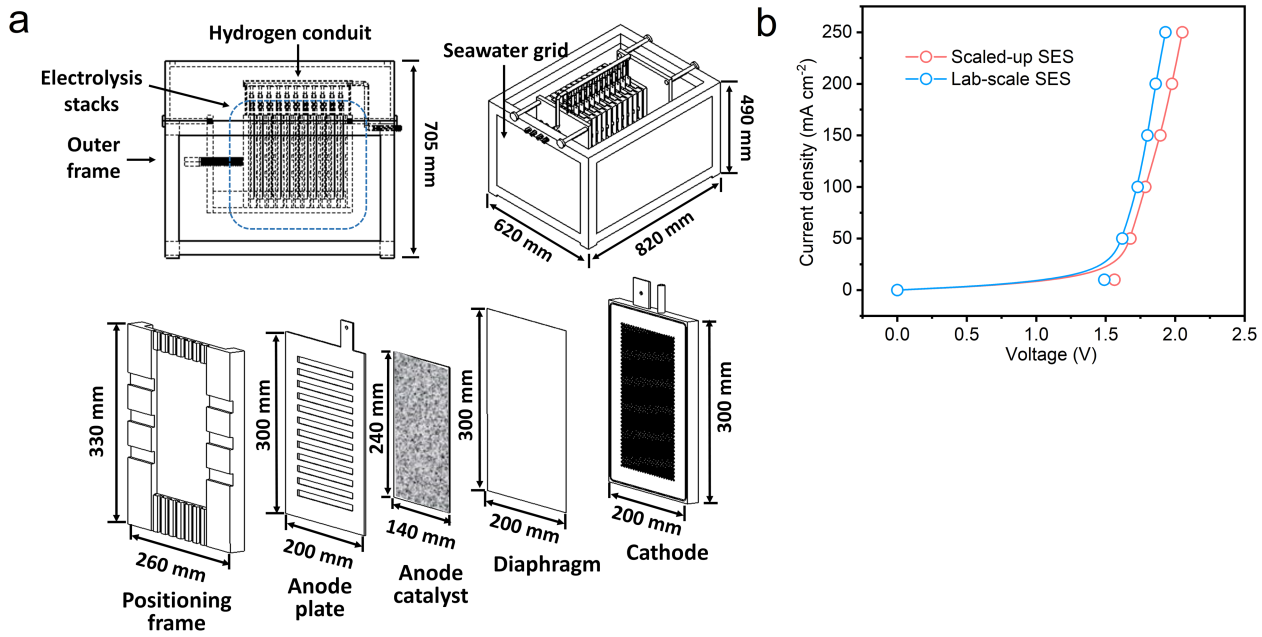

Extended Data Fig. 5 | A schematic diagram and performance of the scaled-up SES. a, The scaled-up SES consists of an electrolytic module composed by 11 cells in parallel. The structure of each cell from left to right: positioning frame, anode plate, MoNi/NF anode catalyst layer, diaphragm, and cathode. The PTFE membrane was lined on the five inner walls of the electrolyser box (except the top) to create a gas path in seawater and hold KOH solution (SDE) at the same time. **b**, LSV curves of the scaled-up SES compared with the lab-scale SES by measuring the voltage at 0, 10, 50, 100, 150, 200 and 250 mA cm^{-2} current densities.

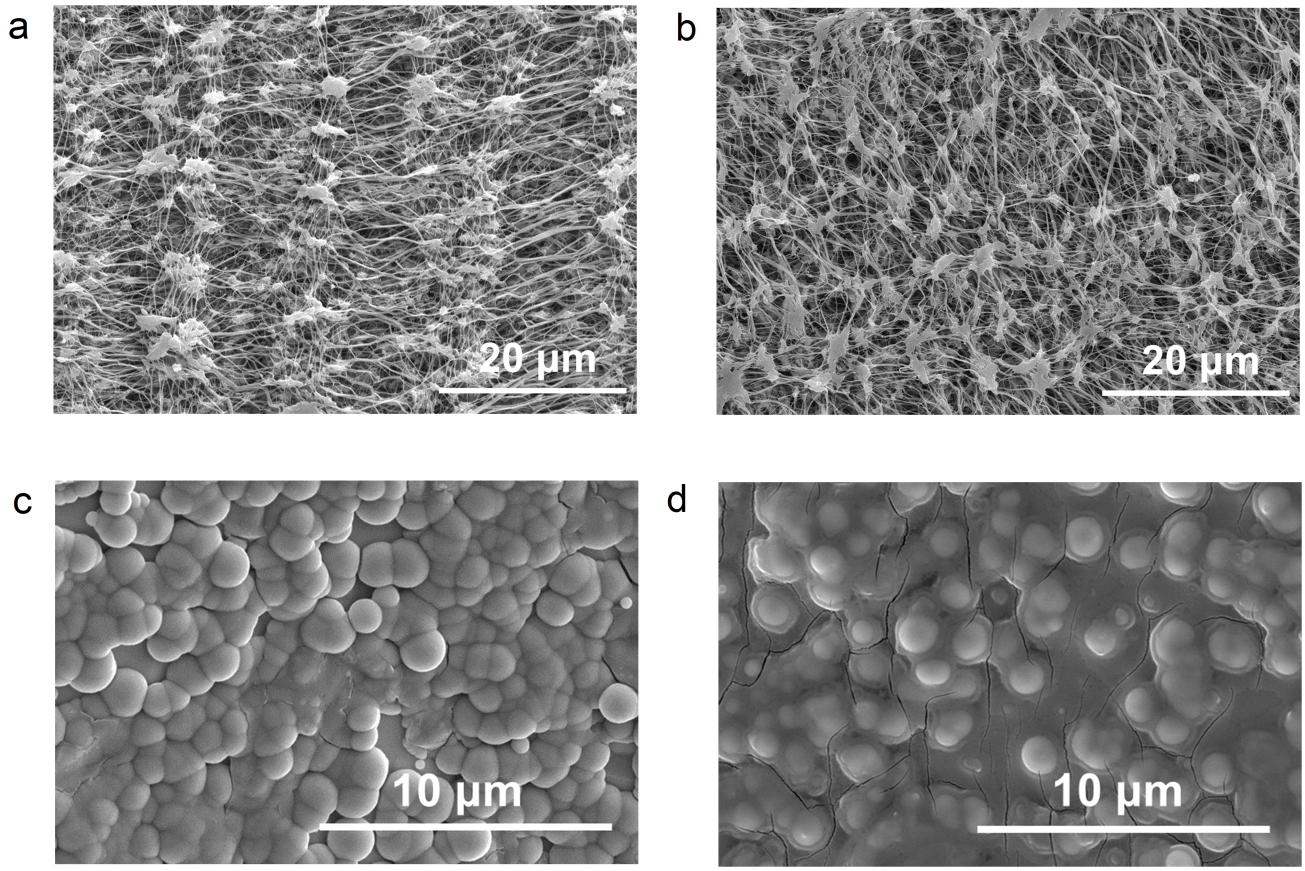

Extended Data Fig. 6 | Fouling and corrosion detection. SEM images of the PTFE membrane before (**a**) and after (**b**) 15 days of electrolysis in SES. SEM images for the MoNi/NF anode catalyst before (**c**) and after (**d**) 200 h electrolysis in a scaled-up SES.

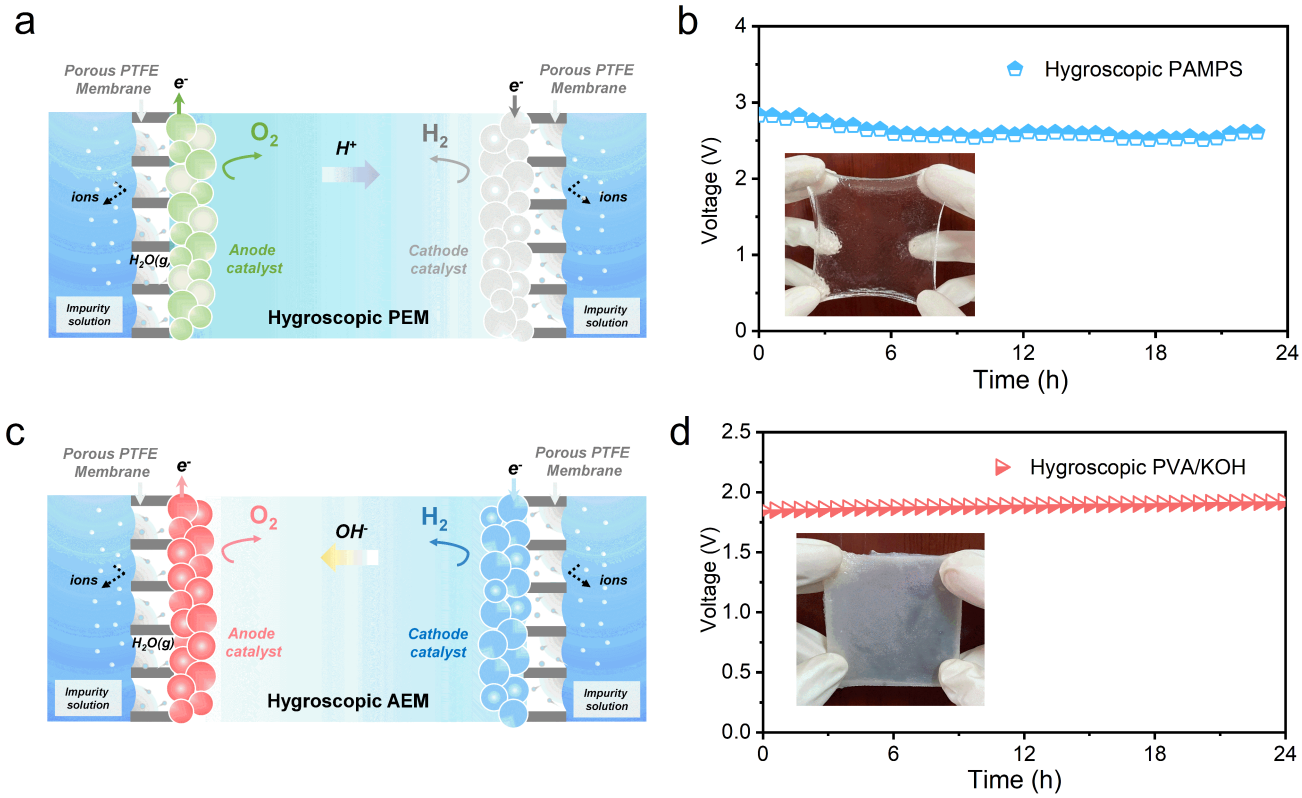

Extended Data Fig. 7 | Hydrogen production of hygroscopic hydrogel SDE. **a**, Schematic of hydrogen production using a hygroscopic PEM based on a phase transition migration mechanism. **b**, Electrolyte durability test for PAMPS at a constant current of 30 mA cm^{-2}. The inset is a diagram of the PAMPS hygroscopic hydrogel SDE. **c**, Schematic of hydrogen production using a hygroscopic AEM based on a phase transition migration mechanism. **d**, Electrolyte durability test for PVA/KOH at a constant current of 250 mA cm^{-2}. The inset is the diagram of the PVA/KOH hygroscopic hydrogel SDE.

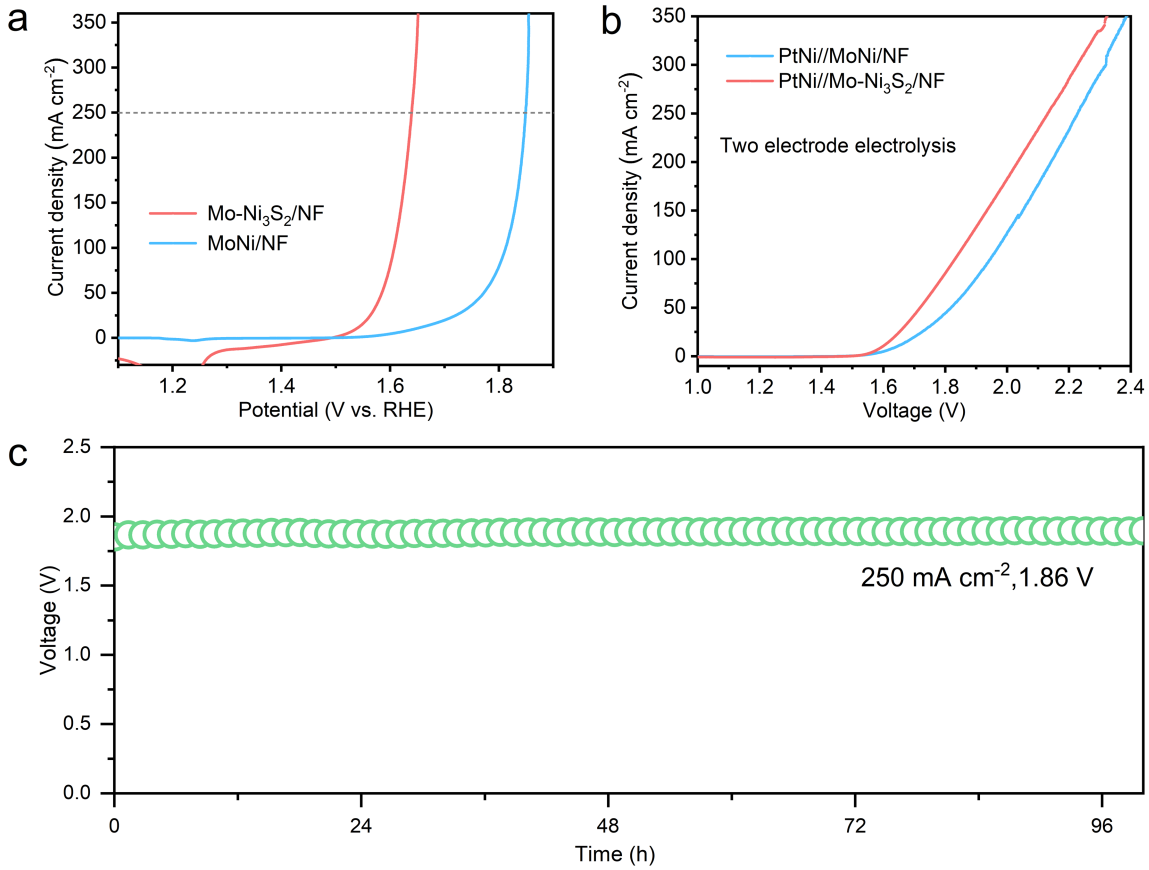

Extended Data Fig. 8 | Performance of SES based on the Mo-Ni_3S_2/NF anode and PtNi mesh cathode. a, OER polarization of Mo-Ni_3S_2/NF and MoNi/NF electrocatalysts in 30-wt% KOH (SDE). **b**, LSV scans of PtNi//Mo-Ni_3S_2/NF and PtNi//MoNi/NF in 30-wt% KOH solution (SDE) (in H-type electrolytic cell). **c**, Seawater electrolysis durability test based on the Mo-Ni_3S_2/NF anode and PtNi mesh cathode at a constant current density of 250 mA cm^{-2} in SES.

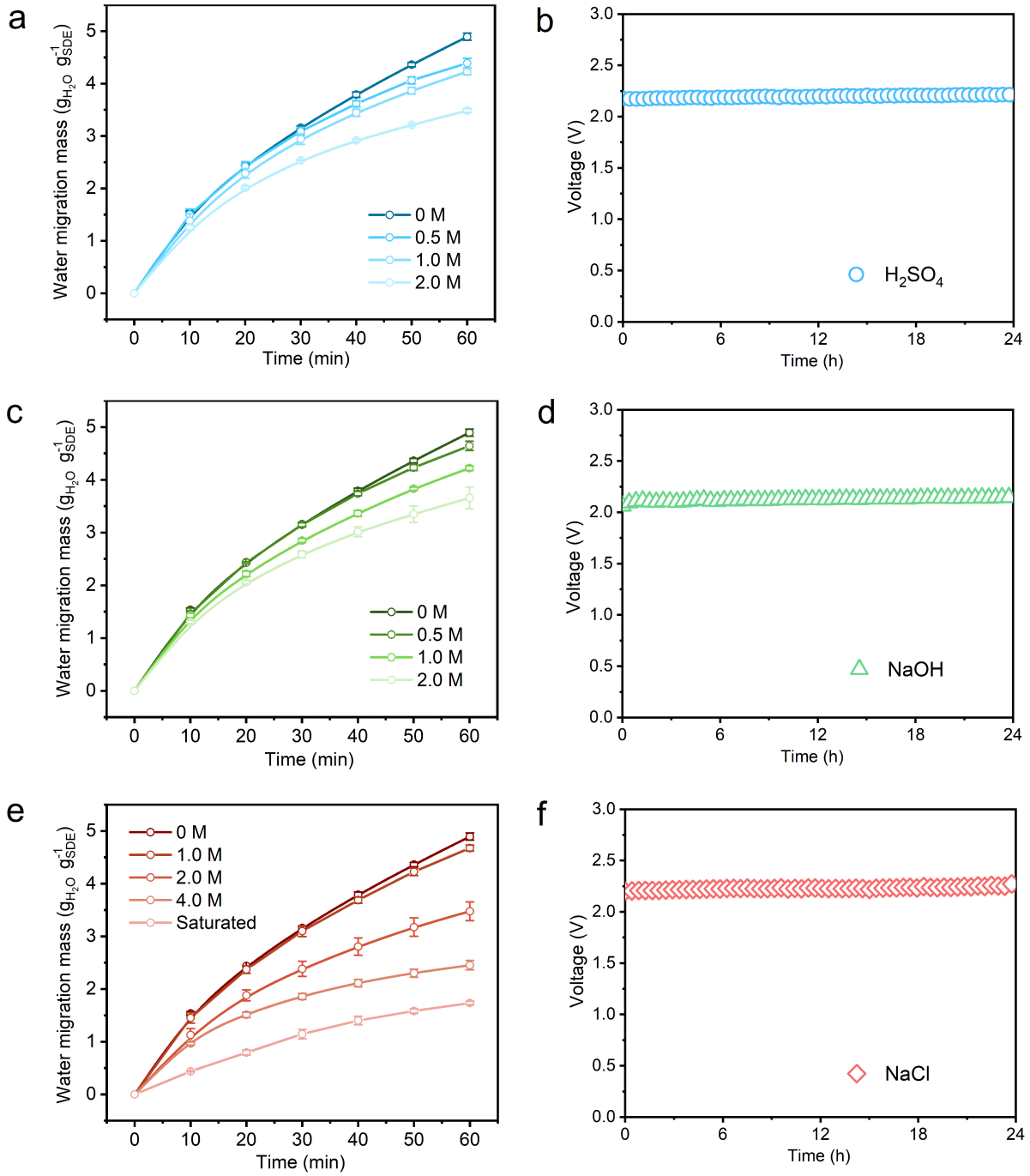

Extended Data Fig. 9 | Application in various impurity water solutions. **a**, Water migration behaviour under different concentrations of H_2SO_4 solution (50 wt% KOH solution as the initial SDE). Each mean value was calculated from three measurements. **b**, Electrolysis durability in 0.5 M H_2SO_4 solution. **c**, The water migration behaviour under different concentration of NaOH solution (50 wt% KOH solution as the initial SDE). Each mean value was calculated from three measurements. **d**, Electrolysis durability in 0.5 M NaOH solution. **e**, The water migration behaviour under different concentrations of NaCl solution (50 wt% KOH solution as the initial SDE). Each mean value was calculated from three measurements. **f**, Electrolysis durability in saturated NaCl solution.

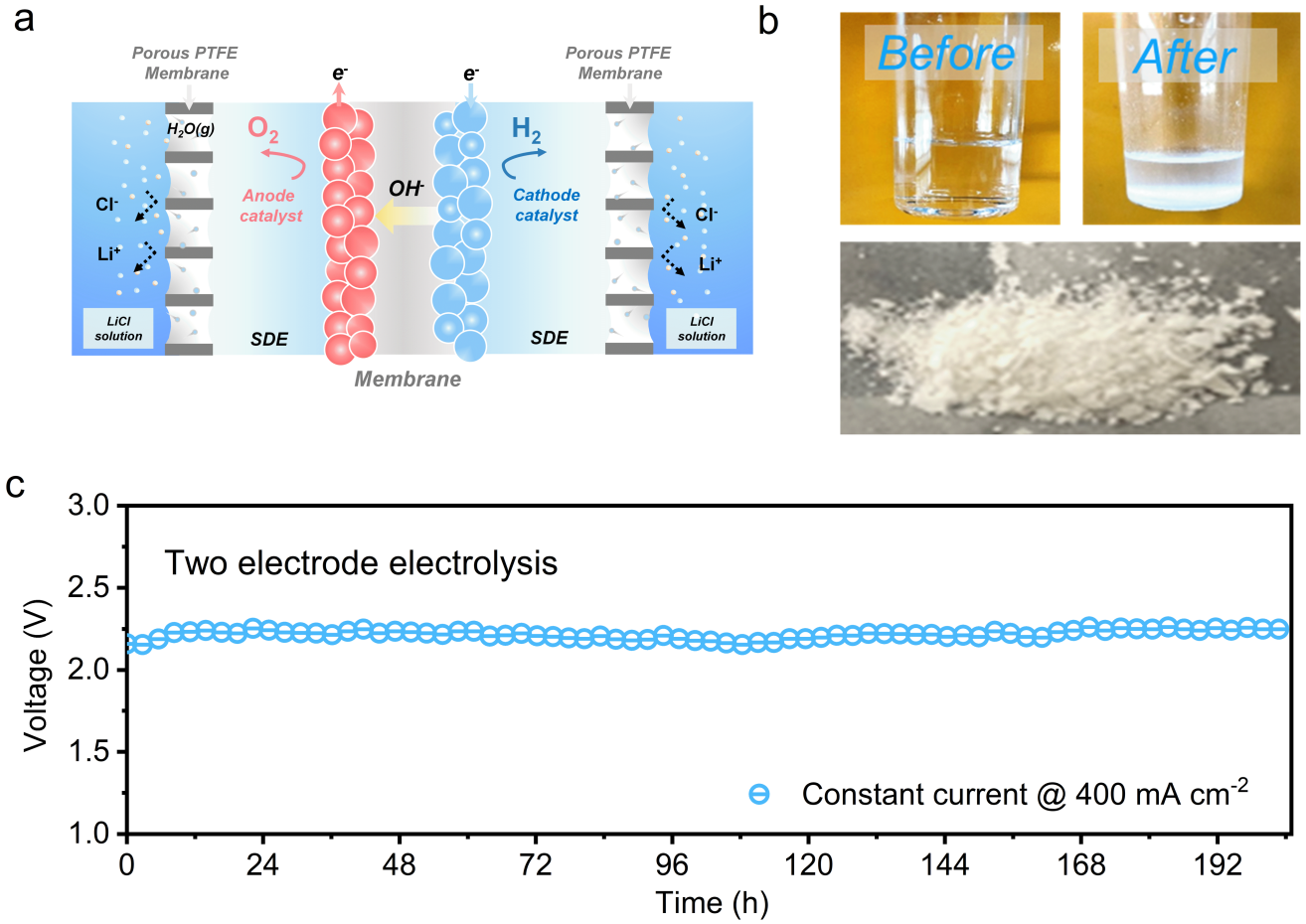

Extended Data Fig. 10 | Lithium enrichment coupled with one-step hydrogen generation based on the phase transition migration mechanism. **a**, Schematic illustration of continuously enriching lithium from the feed solution through water migration and hydrogen generation. **b**, Photos of LiCl solution without precipitation when adding K_2CO_3 solution before concentration, LiCl solution with precipitation when adding K_2CO_3 solution after concentration, and the final Li_2CO_3 production. **c**, Electrolytic durability test for hydrogen production while lithium enrichment at a constant current of 400 mA cm^{-2}.